# Emergent Surface Topography Enabled by Concurrent Crystallization and Polymerization

Mustafa K. Abdelrahman<sup>†</sup>, Hyun Kim<sup>†,‡</sup>, Jimin Maeng<sup>†</sup>, Patrick Ondrusek<sup>†</sup>, Taylor H. Ware<sup>\*,†</sup>

<sup>†</sup>Department of Bioengineering, The University of Texas at Dallas, 800 W Campbell Rd., Richardson, Texas 75080, United States

<sup>‡</sup> Current Address: Sensors and Electron Devices Directorate, CCDC Army Research Laboratory, 2800 Powder Mill Rd., Adelphi, Maryland 20783, United States

Keywords: Surface topography, responsive surfaces, "click chemistry", micro-molding

Materials with dynamic surface topography may enable a variety of new technologies from smart coatings to biomaterials with controlled cell-material interaction. However, current approaches to create morphing surfaces require programming procedures, either before or after polymerization, that complicate the application of these materials. Here, we exploit the metastability of the microstructure of semi-crystalline polymer networks that crystallize while photopolymerizing to create polymer coatings and microstructures that irreversibly morph from smooth to rough in an emergent manner when heated. For example, a smooth polymer coating with a root-mean-square (R<sub>q</sub>) roughness of 15 nm transforms into a rough film with a R<sub>q</sub> roughness of 688 nm on heating through the melt temperature. We show that this behavior is observed across a range of polymer networks and that the degree of undercooling during polymerization is the primary factor that

controls the magnitude of roughness. This technique is not limited to polymer films; microstructures fabricated utilizing micromolding or emulsion polymerization also undergo changes in roughness on heating. Finally, we discuss using this approach to create polymer structures with spatiotemporal control of coefficients of friction and contact angles.

#### Introduction

The surface topography of a material dictates many of the interactions between that material and its environment<sup>1-3</sup>. For this reason, polymeric systems that undergo controlled topographical changes in response to an external stimulus can be used to create smart engineering materials. Dynamically altering the surface topography of polymers using various stimuli such as light<sup>4,5</sup>, heat<sup>6-8</sup>, solvents<sup>9</sup>, or an electric field<sup>10-12</sup> can provide spatiotemporal control over surface wettability<sup>13</sup>, optical properties<sup>14,15</sup>, and liquid transportation<sup>16</sup>. Controlled microscale surface deformations arise in materials or composites where deformation gradients are present at a free surface relative to the bulk or within the bulk of the material<sup>17</sup>. For example, the buckling of a relatively high elastic modulus thin film on a more compliant substrate occurs in response to deformation of the substrate<sup>18–21</sup>. Similarly, the swelling of a compliant coating confined by a rigid substrate causes the formation of wrinkles and creases<sup>22</sup>. These techniques are highly efficient in producing complex and ordered surface features; however, these structures require multi-material processing to generate these smart surfaces.

Dynamic surface topography can also be exhibited in coatings or structures made from only a single material. For example, the shape memory effect can be used to create coatings that undergo topographical transitions<sup>6,7</sup>. As the shape memory effect has been demonstrated in many classes of polymers, this approach provides substantial control over the stimulus required for the surface

topography to be altered. However, mechanical programming is needed to program the metastable geometry, thus limiting the applicability of this process to microstructured surfaces with high complexity, in particular on microscale 3D objects<sup>23-25</sup>. By contrast, liquid crystal networks (LCNs) are mechanically-responsive polymers that do not require a mechanical programming step, and LCNs have been used to create a diverse array of dynamic coatings<sup>4,5,8</sup>. However, dynamic coatings from LCNs require that the monomers exhibit a mesophase and often require a process to orient the mesogenic monomers prior to crosslinking<sup>26</sup>. Strategies are needed to produce materials that undergo transformations in surface topography without requiring programming steps to enable facile fabrication of smart engineering materials across multiple length scales.

Here we present a generic strategy to irreversibly transform the surface topography of semi-crystalline polymer networks from smooth to rough. This emergent roughness is observed when a semi-crystalline polymer network undergoes crystallization during polymerization and is then heated through its crystalline melt temperature. Networks with these characteristics are achieved through a simple radical thiol-ene photopolymerization of commercially-available monomers<sup>27</sup>. This approach is not limited by a programming step; as such, this mechanism can be readily applied to coatings and a variety of microstructures.

## **Experimental Section**

**Materials.** 1,9-nonanedithiol (NDT), diallyl adipate (DAA), 1,7-octadiene (OTD), polydimethylsiloxane (PDMS), and polyvinyl alcohol (PVA) were purchased from Fisher Scientific. 1,6-hexanedithiol (HDT), 1,3-propanedithiol (PDT), and pentaerythritol tetrakis (3-mercaptopropionate) (PETMP) were purchased from Sigma-Aldrich. The photoinitiator, bis (2,4,6-trimethylbenzoyl)-phenylphosphineoxide (I-819), was donated by BASF Corporation. Silicon (Si) wafers were purchased from University Wafers. All reagents were used as received.

Synthesis of Polymer Films An equimolar amount of thiols to alkenes was mixed with 3 wt % of photoinitiator. After adding reagents to a glass vial, the monomer solution was heated with a heat gun to 70 °C for 10 s then vortexed for another 30 s and allowed to cool for 10 min. Cells were prepared by cleaning 2 glass slides (75 mm x 25 mm) and gluing them together using a photopolymerizable adhesive and a 40 µm spacer to set the cell gap. The cell was filled with the monomer solution through capillary action. The solutions were then crosslinked by irradiating with 365 nm UV light with an intensity of 20 mW/cm<sup>2</sup> (Lumen Dynamics, OmniCure LX400+) for 5 min, flipping the sample once. Samples that were crosslinked at temperatures other than room temperature were placed on a hot plate at the desired temperature for at least 10 min before exposure to UV light for 5 min. The sample was then allowed to cool at room temperature. For samples with spatially programmed roughness, the sample was first placed on the hot plate at the highest polymerization temperature for 10 min. UV light was then shone through a mask to only crosslink a portion of the sample for 30 s. Samples were then allowed to cool to room temperature and then flood exposed for 5 min, flipping the sample once. After crosslinking, all samples were annealed at room temperature for at least 12 h before further testing. Gel-fraction was measured by immersing a sample with a mass of ~30 mg in chloroform for 24 h and then drying in a vacuum oven at 60 °C for 24 h. Masses were weighed before immersion into chloroform and after drying with a Sartorius Quintix 125D-1S. All measurements were repeated on 3 samples.

**Thermal Characterization.** Differential scanning calorimetry (DSC) (TA Instruments DSC 2500) was used to measure melt temperature and enthalpy of melt. Sample sizes of at least 1 mg were loaded into aluminum pans and lids and cooled from room temperature to -20 °C, heated to 150 °C, cooled to -90 °C, and then heated back to 150 °C with ramps of  $\pm$  10 °C/min. The enthalpy of melt was calculated from the DSC thermogram by utilizing the enthalpy of melt analyzing tool

within the Trios software<sup>28</sup>. The melt temperature is denoted as the peak of the melting endotherm from the DSC thermograms. All measurements were repeated on 3 samples.

Roughness Measurements. Roughness measurements were gathered using an atomic force microscope (AFM) (Veeco Dimension 500 SPM). Prior to data collection, the upper glass slide was released from the sample. Two AFM scans, with a scan size of 25 µm x 25 µm at a rate of 0.996 Hz, were conducted before and after heating the sample. The sample was heated by placing it on a hot plate set at 10 °C above its melt temperature (Table S1). We note that the heating rate does not significantly affect the magnitude of roughness (Figure S1). All samples were allowed to cool to room temperature before conducting AFM scans. Roughness data and topography images were gathered by utilizing NanoScope Analysis software. Roughness data shown are R<sub>q</sub> roughness. Images shown were 3D renderings after first flattening the image. All measurements were repeated on 3 samples. One-dimensional power spectral analysis was conducted by gathering 6 scans along the same axis of a rough, heated sample of the (75:25:90:10) (OTD:DAA:NDT:PETMP) composition using a DektakXT stylus profilometer. Scan lengths were 500 µm with a duration of 240 s and a stylus force of 1 mg. Data was then leveled using Gwyddion software. Power spectrum density was computed utilizing the Welch method for each scan and then averaging the calculated power spectrums using Matlab code<sup>29,30</sup>. Data was smoothed through an adjacent averaging method, considering 50 points, and plotted on a log-log scale.

**Microscopy.** Optical microscopy was performed with a polarizing optical microscope (POM) (Olympus, BX51). Crystallite formation was observed by *in-situ* crosslinking of monomer solution in a cell in the POM. Crosslinking was performed with the broadband halogen bulb used in transmission mode microscopy. The sample was irradiated in 1 s intervals for 3 s. The light intensity of the visible light used for polymerization was 4 mW/cm<sup>2</sup>. Images were taken after each

increment. In order to block light from further polymerizing while imaging in transmission mode through crossed polarizers, a long pass filter was used that blocks light below 610 nm. Videos of crystallization during polymerization were taken utilizing a similar method, but the sample was irradiated in a continuous manner. Surface deformation videos were imaged by first placing the sample on a thermal heat stage (Linkam) and viewing the sample in darkfield reflection mode. The temperature was increased at 10 °C increments at a rate of 50 °C/min from room temperature to 10 °C above the melt temperature, as measured by DSC. A scanning electron microscope (SEM) (Zeiss Supra 40) was used to observe the surface deformation of 3D structures. Prior to imaging, samples were sputtered with 76 Å of gold mixed with palladium. Samples were imaged before and after heating. Micro-rectangular prisms and microneedles were imaged at a tilt angle of 30°.

X-ray Diffraction. Wide-angle X-ray scattering (WAXS) was performed at ambient temperatures using an X-ray diffractometer (Rigaku, SmartLab) with a Cu Kα radiation source, having a wavelength of 1.54 Å and operating at 44 kV and 44 mA. Diffraction patterns were then obtained over a 2θ range of 5° - 50° at a scan rate of 5°/min with a resolution of 0.01°. Diffraction curves were smoothed through an adjacent averaging method, considering 10 points. Baselines were then subtracted through a baseline fitting method utilizing 3D Explore, an analytical software package provided by Rigaku. Next, the areas of multiple crystalline peaks were calculated by utilizing a Lorentz curve fitting method in Origin Pro. The crystalline fraction was calculated from the ratio of the area of the crystalline peaks to the total peak area using Origin Pro.

**Measuring Friction.** Friction measurements were gathered through a home-built system (Figure S2). A dynamic mechanical analyzer (DMA) (TA Instruments, RSA-G2) was used to measure force vs. displacement curves by pulling one sample across another sample. The bottom sample was 75 mm x 25 mm, while the top sample was 10 mm x 10 mm. Both samples were adhered to

glass slides on one side. The top substrate was pulled across the bottom stationary substrate, with coatings facing each other, at a rate of 0.1 mm/s. A mass was placed on the top sample (0.021 kg). The home-built system was validated by using known glass on glass coefficient of friction values. After running the smooth unheated samples across each other, those same samples were heated on a heat stage and roughness was confirmed through optical microscopy. Before conducting tests with the heated samples, the samples were allowed to cool for at least 10 min. Coefficient of kinetic friction ( $\mu_k$ ) was calculated through this equation:  $\mu_k = \frac{F_{friction}}{N}$ , where  $F_{friction}$  is the average force values attained from the force vs. displacement curve and  $N = Mass \times 9.8 \ m/s^2$ .

**Synthesis of Microspheres.** Microspheres were synthesized by first creating an emulsion with a 10:1 ratio of 8% PVA in water solution to monomer solution. The emulsion was subsequently crosslinked by irradiating with 365 nm UV light with an intensity of 20 mW/cm² for 2 min. Following crosslinking, particles were washed by centrifuging for 3 min, removing supernatant, and adding DI water repeatedly for three cycles. After washing, microspheres were suspended in DI water.

Preparation of Microstructures. Micro-rectangular prisms were fabricated through the use of a silicon (Si)-based micromold. The silicon micromold was fabricated by photolithography and deep reactive ion etching (DRIE). A positive photoresist (S1827) layer of 4 μm thick was spin-coated on 3 inch Si wafers and micropatterned to serve as an etch mask. An inductively coupled plasma (ICP) etching system (Plasma-Therm ICP etcher) was used for Si DRIE. SF<sub>6</sub> and C<sub>4</sub>F<sub>8</sub> gases were employed to enable cyclic etching and passivation through quick gas switching. A plasma power of 1200 Watts and a DC bias of 250 Volts were used for the etching cycle. The total Si etch depth was about 100 μm. After the DRIE process, the Si micromolds were cleaned using acetone and isopropyl alcohol. The molds were then sandwiched with a microscope glass slide (75 mm x 25

mm) and a spacer of a 100 µm to set the cell gap thickness. The mold was then filled with the monomer solution through capillary action. After filling, the mold was irradiated with 365 nm UV light with an intensity of 20 mW/cm<sup>2</sup> for 150 s with the glass side facing the UV source. The sample was subsequently removed from the mold and irradiated with 365 nm UV light for 150 s with the microstructures facing the UV source. Microneedles were fabricated through a known process of ablating PDMS with a CO<sub>2</sub> laser engraver<sup>31</sup>. Briefly, a PDMS mold was prepared by mixing PDMS in a 10:1 weight ratio and casting into a custom mold to produce a 15 mm x 15 mm x 4 mm PDMS substrate with a 12 mm x 12 mm x 1 mm indentation in the center. The PDMS was then degassed under vacuum for 1 h and cured at 80 °C for 3 h in an oven. A CO<sub>2</sub> laser engraving machine (Universal Laser Systems ILS9.150D) was used to ablate an 8 x 8 array of 0.06 mm circles into the PDMS mold in order to create a microneedle array into the PDMS. The PDMS micromold was subsequently plasma treated, sandwiched between two glass slides, and clamped together using bulldog binder clips, leaving a small opening to allow the monomer solution to enter. After filling mold with monomer solution, the sample was placed under vacuum for 2 minutes. Subsequently, the sample was irradiated with 365 nm UV light with an intensity of 20 mW/cm<sup>2</sup> for 150 s with the base of the microneedles facing the UV source. Afterward, the PDMS was removed, leaving the sample adhered to the glass slide. The sample was then irradiated with 365 nm UV light for 150 s with the microneedle tips facing the UV source.

Contact Angle Measurements. Contact angles were measured using a Ramé-Hart model 50-00-115. For each sample, a 2 µl water droplet was placed on the surface and allowed to equilibrate for 2 s. Contact angles were measured at 3 locations. The sample was then heated to its melt temperature and allowed to cool for 10 min. The contact angles were then measured at 3 locations.

### **Results and Discussion**

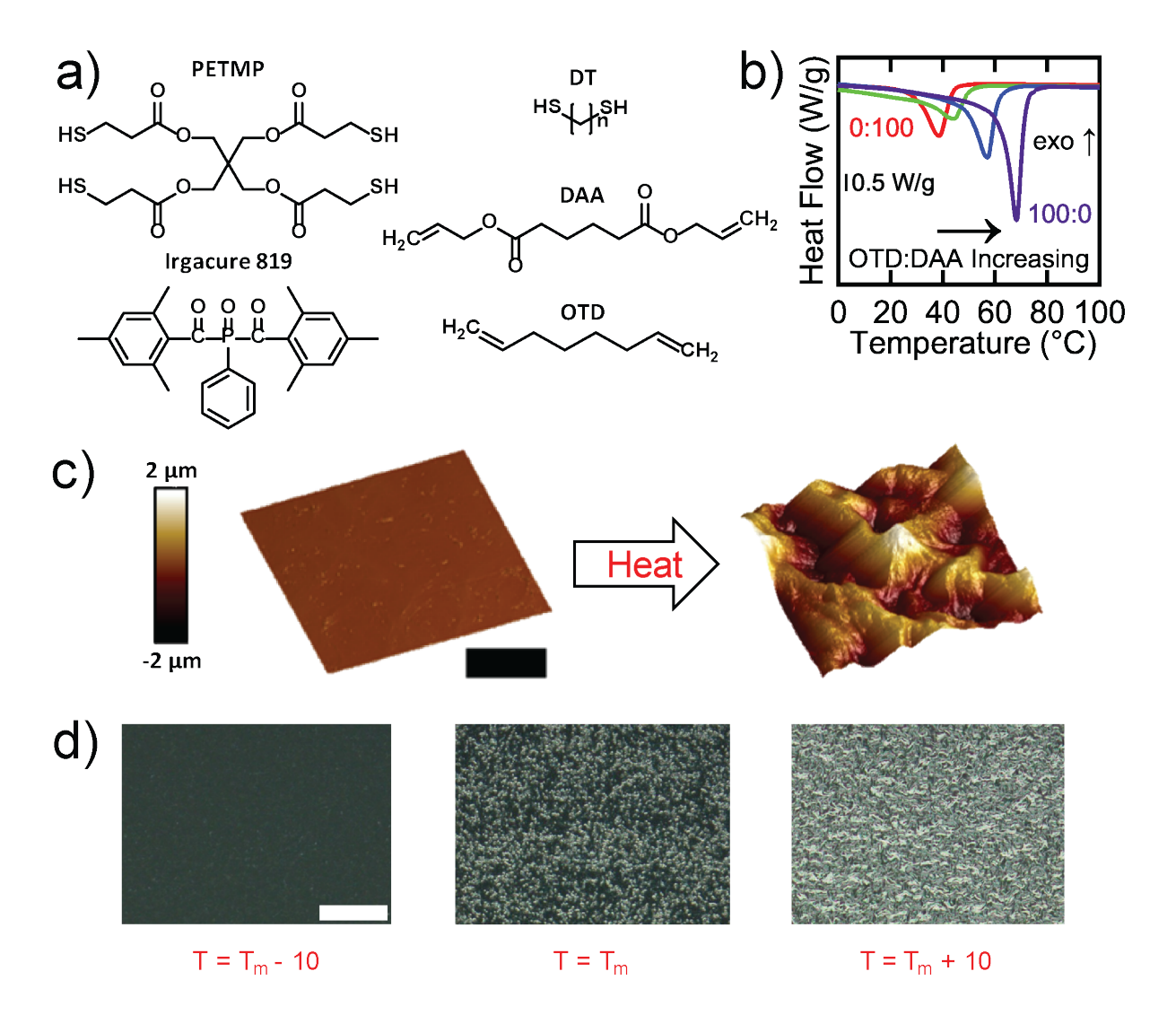


**Figure 1.** a) Molecular structures of monomers used to synthesize semi-crystalline polymers. b) Representative DSC thermograms of the second heating cycle showing tunable melt temperatures by altering OTD:DAA ratio. c) Atomic force micrographs showing a smooth surface transforming into a rough surface on heating through the melt temperature. Scale bar: 5 μm. d) Darkfield reflection optical micrographs showing the appearance of roughness at the melt temperature and an increase of roughness  $10~^{\circ}$ C above the melt temperature ( $T_m$ ). Scale bar:  $50~\mu m$ .

To synthesize a series of semi-crystalline polymer networks, we chose to use the radical photopolymerization of divinyl, dithiol (DT), and tetrathiol monomers. The monomers, PETMP, a DT, DAA, OTD, and photoinitiator, I 819, are shown in Figure 1a. This system allows for broad control of phase transition temperatures. For example, the melt temperature (Figure 1b) can be broadly controlled from 39 - 68 °C and the degree of crystallinity (Figure S3) increases by increasing the ratio of OTD to DAA while keeping the molar ratios of other monomers fixed at (X:100-X:90:10) (OTD:DAA:NDT:PETMP). When polymerized at room temperature, each of these materials is smooth. Unexpectedly, on heating above the crystalline melt temperature, each material becomes rough (Movie S1). At a molar ratio of 100:0 (OTD:DAA), the smooth polymer film obtained after polymerization, with a Rq roughness of 15 nm, is transformed into a rough surface with a R<sub>q</sub> of 688 nm, through heating to 78 °C (Figure 1b, c, d, Table S1). Surface roughness begins to emerge at the melt temperature; however, the maximum roughness is not achieved until heating completely through the melting transition. After cooling, the surface remains rough. We note that rough samples do not return to the original smooth topography for at least three months after heating (Figure S4). To our knowledge, this phenomenon has not been previously reported. As such, we sought to elucidate the origins of this phenomenon and to provide approaches to control this mechanism.

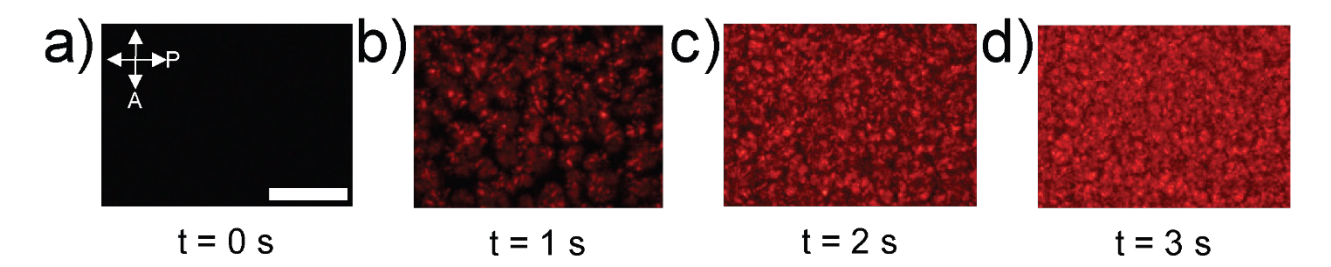


**Figure 2.** Transmission optical micrographs between crossed polarizers during *in-situ* photopolymerization of (75:25:90:10) (OTD:DAA:NDT:PETMP) monomer solution polymerized

33 °C below  $T_m$  demonstrates crystallization after exposure to visible light at increments of t=0, 1, 2, and 3 s. Scale bar: 50  $\mu m$ .

A key distinction between the reported thiol-ene semi-crystalline networks and many other semi-crystalline polymers is that crystallization occurs concurrently with photopolymerization when the monomers are irradiated at temperatures below the melt temperature of the final network<sup>32</sup>. The concurrent polymerization and crystallization of these series of materials were observed using polarized optical microscopy during photopolymerization of the initially isotropic monomer solution (Figure 2a). Even at low intensities of visible light, within 1 s of photopolymerization (Figure 2b, Movie S2), crystallites begin forming, as indicated by the appearance of birefringent regions within the solution. As photopolymerization continues spherulites grow and eventually occupy a significant fraction of the polymer (Figure 2b-d).

Materials that crystallize while polymerizing exhibit polymorphism, giving rise to metastable crystalline structures and morphologies<sup>33–35</sup>. Since the early 1970s, it has been documented that after polymerization of para-xylylene derivatives, non-reversible changes in crystalline structure are observed upon either the extraction of solvent or annealing<sup>33–38</sup>. There are two likely reasons why such phenomena occur. First, crystals growing directly from solution or melt are prone to defects<sup>34</sup>. Second, due to reaction kinetics, there is an inverse relationship between defects found in crystals and the polymerization temperature<sup>34</sup>. Herein there exists a similar change in the crystal structure after heating above the melt temperature (Figure S5a,b). The diffraction pattern of the (75:25:90:10) (OTD:DAA:NDT:PETMP) sample polymerized at room temperature (33 °C below the melt temperature) illustrates a significant change in crystal structure after heating. After synthesis, prominent peaks exist at  $2\theta = 19.4^{\circ}$ ,  $23.31^{\circ}$ , and  $25.15^{\circ}$ . However, after heating through the melt temperature, the peaks at  $2\theta = 23.31^{\circ}$  and  $25.15^{\circ}$  are significantly reduced. This suggests

a decrease in crystallinity and a change in the crystalline structure. We hypothesize that this change in crystal structure and spatially-varied polymerization stress are responsible for the emergent topographical deformation observed on melting the polymer network. We believe heterogeneous polymerization stress arises as different regions of the sample crosslink and crystallize during polymerization. On heating, these crystallites melt and the heterogeneous polymerization stress is resolved by forming surface topography. This is analogous to macroscopic heterogeneous polymerization stress that can occur in the polymerization of thermosets, which can cause warping<sup>39–41</sup>.

To further understand the origin of surface deformations, a composition of (0:100:90:10) (OTD:DAA:NDT:PETMP) was synthesized and polymerized at room temperature ( $T_p - T_m = -17$ °C). This composition produces a semi-crystalline polymer with a melt temperature of 37 °C (Figure 1b, Table S1). As the degree of undercooling is relatively low, this polymer network crystallizes with large spherulites, rendering them easier to study. Before heating, the outline of each crystallite is clearly imprinted on the surface of the polymer (Figure S6a,b). However, after heating through the crystalline melt, a protruding structure forms in the center of each crystallite, with wave-like patterns approaching the spherulite border (Figure S6c,d). At smaller spherulite sizes, the deformation associated with melting a single spherulite is difficult to observe. However, we expect similar deformations produced by many spherulites to lead to an increase in surface roughness for materials polymerized with larger degrees of undercooling. As surface roughness was observed to exist on both the micrometer and the nanometer scale (Figure S7, S6d), power spectral analysis was conducted. The generated rough surfaces exhibit both fractal and periodic regions, suggesting two coexisting morphology length scales<sup>30</sup> (Figure S8). We note that structures resembling crystal slip deformations are observed in AFM scans of higher resolution<sup>42</sup> (Figure S7).

As this roughening phenomenon appears to be general to this class of polymer networks, we sought to control the magnitude of roughness transformation and triggering temperature using both process variables and monomer selection.

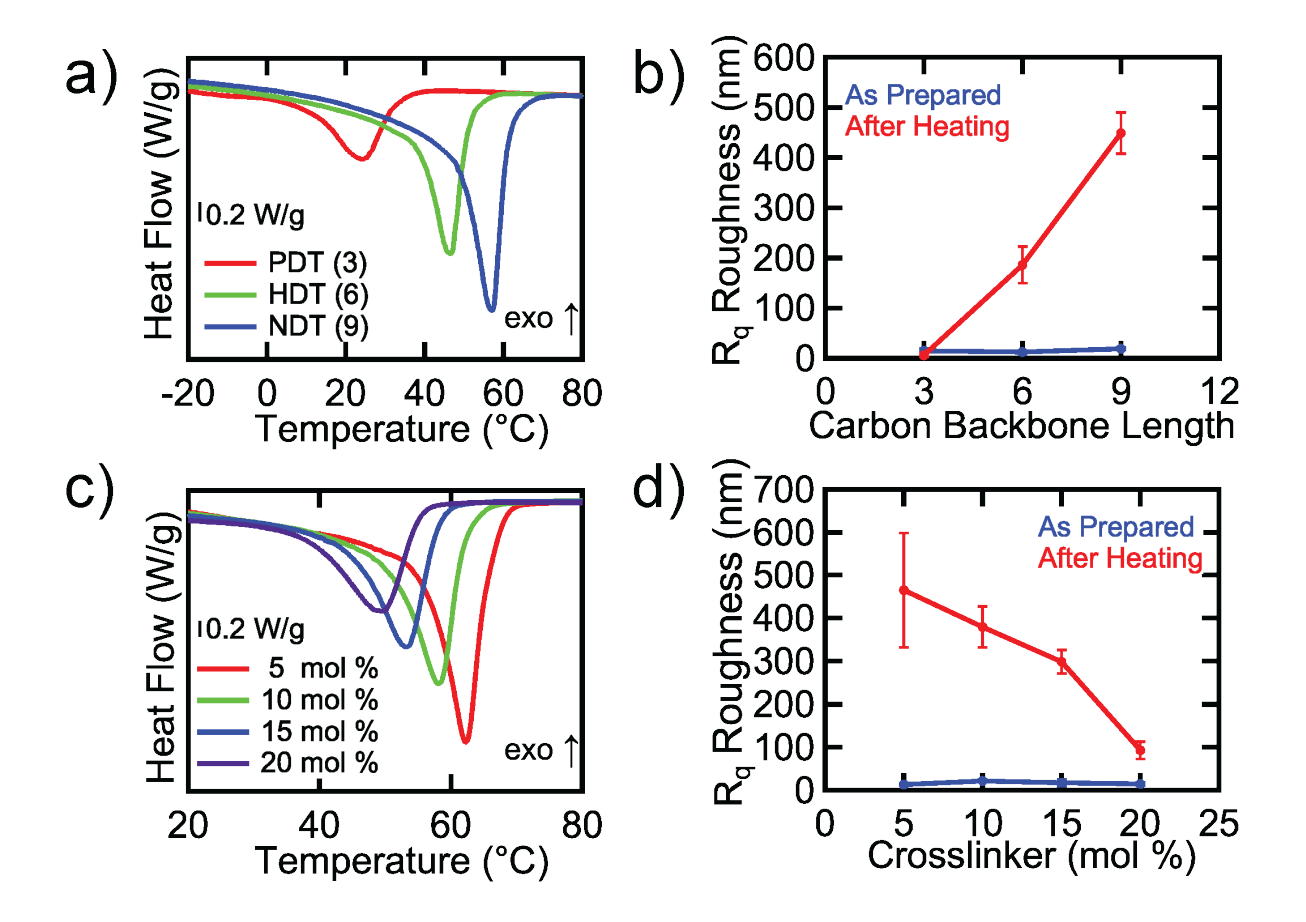
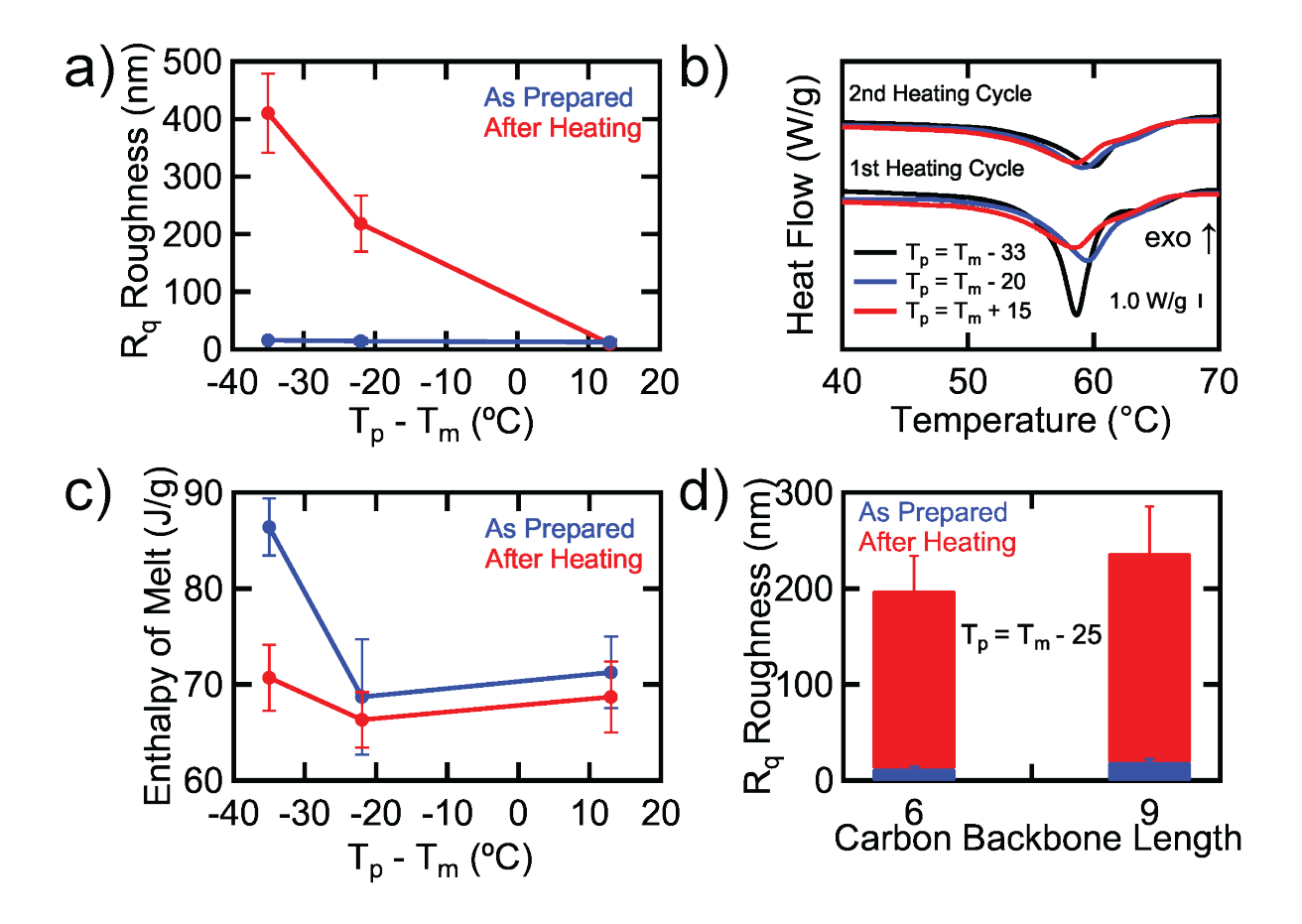


Figure 3. Monomer composition controls roughness and melt temperature. a) Representative DSC thermogram of the second heating cycle demonstrating tunable melt temperatures by altering thiol chain extender from PDT to HDT to NDT. b) Roughness plotted against the carbon backbone length of each chain extender (PDT, HDT, NDT). c) Representative DSC thermogram of the second heating cycle demonstrating tunable melt temperatures by altering the crosslinker (PETMP) mol %. d) Roughness plotted against crosslinker (PETMP) mol %. For plots b and d, each data point represents the mean (n=3) and the error bars represent the standard deviation. Lines between points are added to guide the eye.

Monomer selection and monomer feed ratios can be used to control both the degree of roughness achieved and the response temperature of these polymer networks. For example, higher concentrations of OTD increase the melt temperature of the network (Figure 1b). By altering the molar ratio of OTD to DAA from 0:100 to 100:0, the roughness after heating through the melt temperature can be tuned from 32 nm to 546 nm (Figure S3b). Similar control can be obtained by altering the DT or the crosslinker concentration within the network. Altering the length of the alkyl DT from PDT to HDT to NDT, while keeping the molar ratios of other monomers fixed at (75:25:90:10) (OTD:DAA:DT:PETMP), increased the melt temperature from 24 °C to 57 °C (Figure 3a, Table S1). Roughness after heating also increased from 6 nm to 449 nm (Figure 3b). Additionally, crosslink density can be used to control the degree of roughness. Altering the crosslinker feed ratio from 5 mol% up to 20 mol%, while keeping the molar ratios of other monomers fixed at (75:25:100-X:X) (OTD:DAA:NDT:PETMP), caused a decrease in both the response temperature and the degree of roughness (Figure 3c,d, Table S1). At 5 mol% of crosslinker, roughness is 465 nm after heating, and the response temperature is 63 °C. At 20 mol% of crosslinker, roughness after heating is 93 nm, and the response temperature is 50 °C. We note that all of these networks are crosslinked with gel fractions greater than 75 % for compositions with 10 mol% PETMP or greater (Figure S9). By changing monomers used, a clear coupling of chemistry and processing variables appears. Networks with lower crystallinity (as measured by the enthalpy of melt) also melt at lower temperatures, which in turn have a smaller difference in temperature between the melt temperature and the polymerization temperature. To decouple these effects, processing variables are changed within a single composition.



**Figure 4.** Polymerization temperature affects surface roughness. a) Roughness plotted against polymerization temperature – melt temperature ( $T_p - T_m$ ), as measured by AFM. b) Representative DSC thermograms demonstrating the difference between the first and second heating cycles. c) Enthalpy of melt before and after heating the samples plotted against  $T_p - T_m$  demonstrating a decrease in crystallinity before and after heating to the melt temperature, as measured from DSC thermograms. d) Roughness of films prepared with HDT and NDT while keeping molar ratios fixed at (75:25:90:10) (OTD:DAA:DT:PETMP) polymerized at  $T_p - T_m = -25$  °C demonstrating similar degrees of roughness, as measured by AFM. For plots a, c, and d, each data point represents the mean (n=3) and the error bars represent the standard deviation. Lines between points are added to guide the eye.

By polymerizing a single composition, (75:25:90:10) (OTD:DAA:NDT:PETMP), at temperatures below and above the melt temperature, the degree of roughness after heating can be tuned independently of composition (Figure 4a). By polymerizing from 33 °C below the melt temperature to 15 °C above the melt temperature, the roughness after heating can be tuned from 410 nm to 9 nm. We note that for larger degrees of undercooling, there exists a significant reduction in the degree of crystallinity after heating through the melt temperature (Figure 4b,c, S5c). Polymerization kinetics were analyzed by observing the crystallization speed of samples polymerized at 33 °C, 25 °C, and 15 °C below the melt temperature. For samples polymerized 33 °C below the melt temperature, spherulites begin forming after 1 s; however, for samples polymerized at 25 °C and 15 °C below the melt temperature, spherulites began forming after 8 s and 14 s, signifying a significant decrease in the rate of crystallization (Figure 2, Movie S1). For networks where spherulites form significantly quicker during polymerization, there are more sources of incompatible stresses within the material. It is also expected for there to be defects in the crystalline structure. As previously mentioned, the diffraction patterns observed before and after the first melt signify a change in the crystalline structure for samples polymerized at higher degrees of undercooling, while patterns largely remain the same for samples polymerized above or just below the melt temperature of the network (Figure S5a, b).

Differences in morphology of samples polymerized with varying degrees of undercooling are observed through AFM phase and height images (Figure S10). For samples polymerized at 33 °C below the melt temperature, we notice significant contrast in the phase images which is indicative of mechanical heterogeneity. Additionally, height images show preexisting surface deformation, which was also observed through bright field microscopy (Figure S10, S6b). However, for samples polymerized at 15 °C above the melt temperature, we do not see these same structures nor signs

of mechanical heterogeneity. The source of mechanical heterogeneity observed on samples with higher degrees of undercooling is likely attributed to concurrent crystallization and polymerization that is observed when polymerizing below the melt temperature.

Notably, networks with distinct enthalpies of melt before heating, and likely different degrees of crystallinity, such as those formed with NDT (68.7 J/g) or HDT (59.2 J/g), each polymerized 25 °C below the respective melt temperature of each network yield similar surface roughness after heating (Figure 4c, d, S3c). While the polymer network must crystallize during polymerization to enable heating induced roughening, ultimately the degree of undercooling appears to dictate the magnitude of roughness.

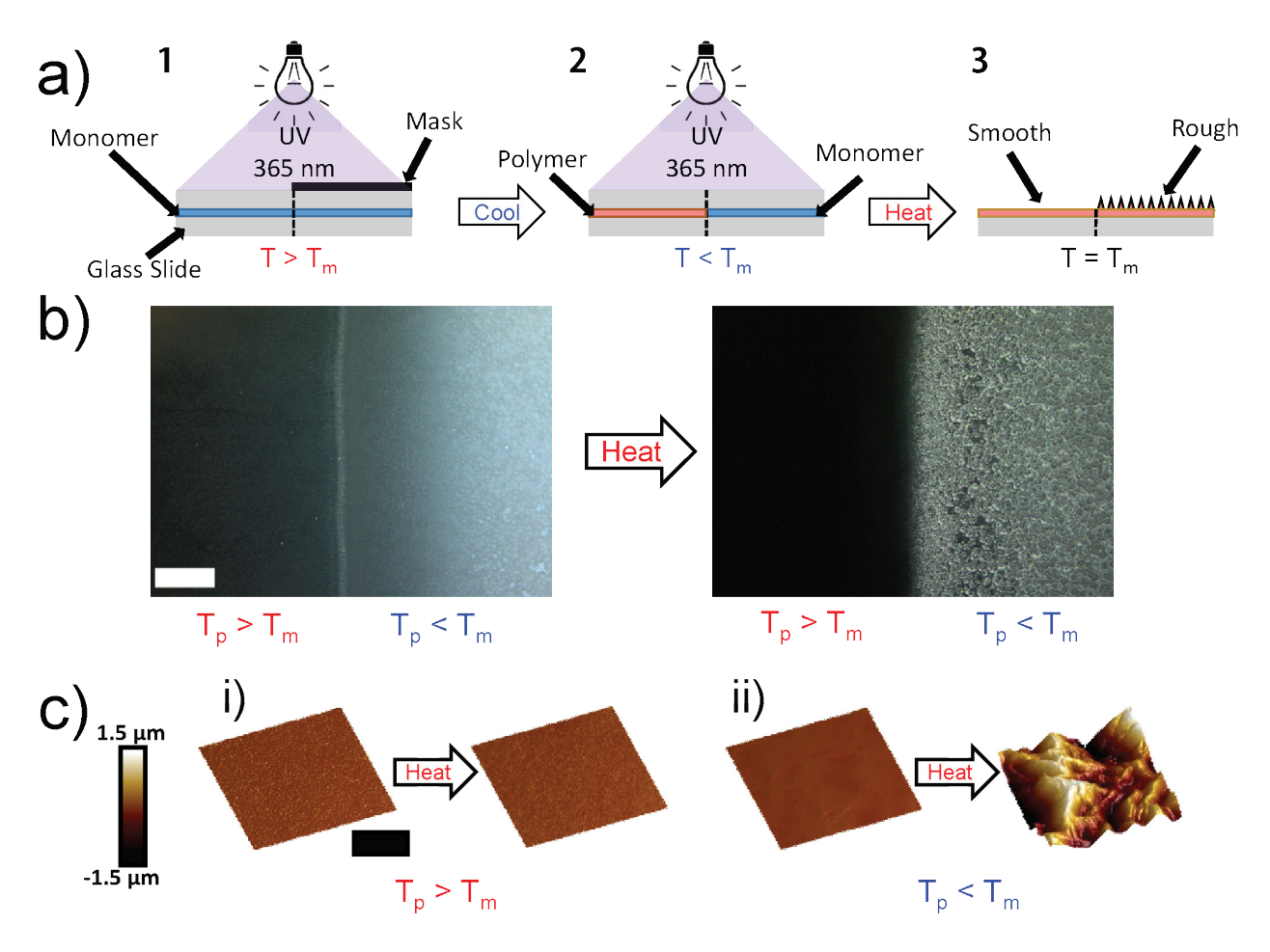
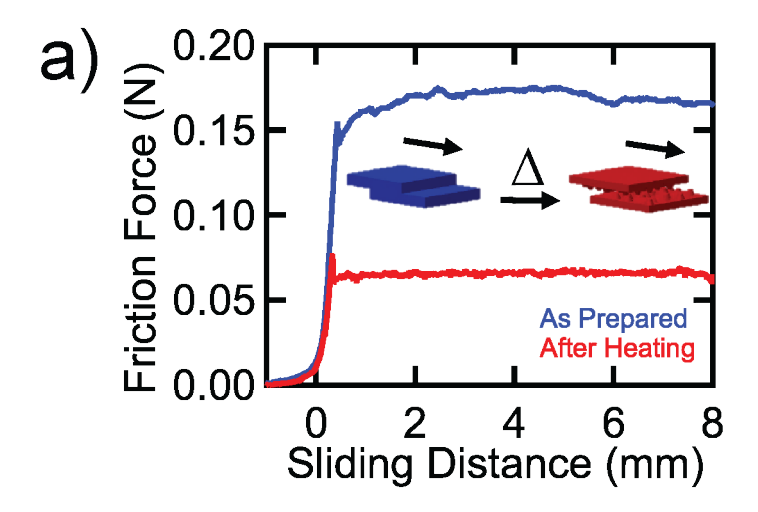


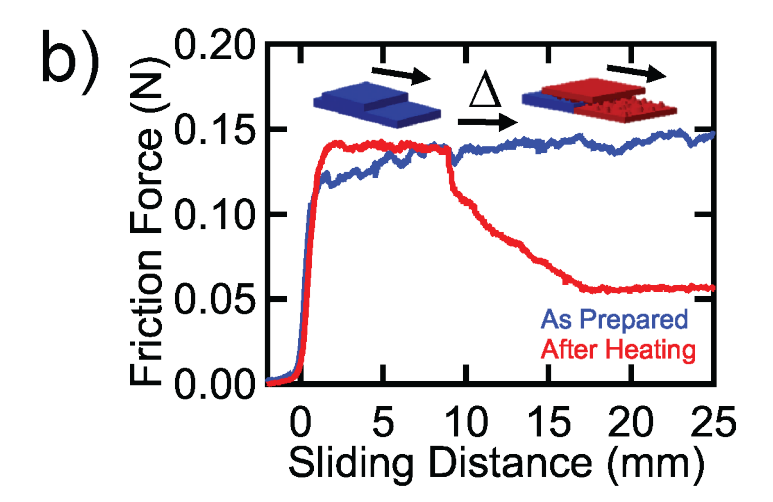
**Figure 5.** Spatiotemporal programming of surface roughness. a) Schematic demonstrating procedure of spatiotemporally controlling roughness. b) Darkfield reflection optical micrographs

demonstrating spatiotemporal control of roughness after heating. Scale bar: 200  $\mu$ m. c) Regions polymerized above  $T_m$  (i) remain smooth on heating while regions polymerized below  $T_m$  (ii) become rough. Scale bar: 5  $\mu$ m.

Photopolymerization enables patterning of the polymerization temperature, which in turn enables spatially-programmed surface deformations. To achieve this patterning, portions of films can be polymerized above the melt temperature, while other portions are polymerized below the melt temperature (Figure 5a). As expected, the portion of the sample that was crosslinked above the melt temperature ( $T_p - T_m = 15~^{\circ}\text{C}$ ) does not become rough upon heating, while the portion of the sample that was crosslinked below the melt temperature  $(T_p - T_m = -33 \ ^{\circ}\text{C})$  becomes rough, as can be observed in darkfield microscopy or AFM (Figure 5b,c, Movie S3). Notably, this phenomenon does not require intricate programming steps, as is the case with other techniques for producing controllable topographical deformations. This allows for a facile mechanism to control polymeric surfaces, which will prove useful for developing substrates with dynamic control over the properties of friction and contact angles (Figure S11, Movie S4). We note that the spatial resolution of patterning is limited, as the formation of spherulites causes light to scatter and further photopolymerize surrounding areas. However, polymerization of structures with dimensions approaching 100 μm has been achieved. By utilizing a photomask with feature sizes that approach the size of the spherulites of the (0:100:90:10) (OTD:DAA:NDT:PETMP) composition (Figure S6a), aligned crystals are formed as evident by uniform birefringence (Figure S12). However, no obvious change in topography is observed from these oriented structures on heating. We expect that there must exist multiple spherulites to induce a topographical deformation on heating. Aligning crystallites through this methodology could prove to be quite useful for many

applications; however, it is out of the scope of the present work and has been reserved for future studies.





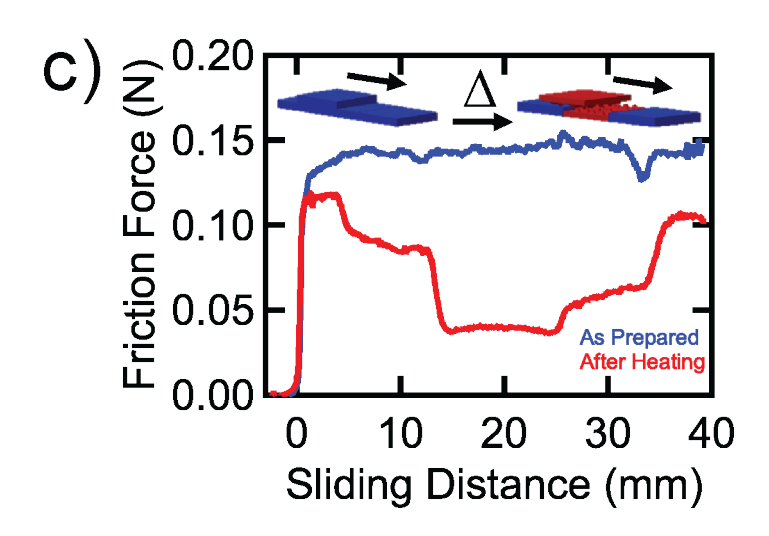


**Figure 6.** Roughness dictates the coefficient of kinetic friction. Dynamic force traces showing friction force before and after heating an a) unprogrammed sample, b) sample that is programmed to turn rough only on half of the sample, and c) sample that is programmed to turn rough only in the middle of the sample. (75:25:90:10) (OTD:DAA:NDT:PETMP) composition was used. The arrows above each schematic illustrate the sliding direction of the top sample across the bottom stationary sample.

Imprinting micro-textures and corrugations onto polymeric substrates has been demonstrated to alter the coefficient of friction<sup>43,44</sup>. Dynamic control of friction is quite useful, especially for developing materials with self-cleaning capabilities and dynamic adhesive properties 10,45. Heatinginduced roughness dramatically changes the coefficient of kinetic friction between two polymer networks of the same composition (Figure 6a). Before heating the two samples,  $\mu_k$  between the two smooth samples was measured to be 0.8. However, after heating the two samples,  $\mu_k$  between the two rough samples was measured to be 0.3, signifying a 62.5% reduction (Figure 6a). Spatial control of  $\mu_k$  can be generated by patterning the polymerization temperature of the polymer, as demonstrated in Figure 6b and Figure 6c. In Figure 6b, one polymer film morphs from smooth to rough, while the other only transforms from smooth to rough on half of the film. As such, the friction force dramatically decreases as the rough sample transitions from contact with a smooth surface to a rough surface. In Figure 6c, the bottom sample is patterned to have a single rough section in the middle of the film surrounded by two smooth sections. As a result, the initially high friction force decreases and then increases as the two films slide over one another. Notably, each of these films exhibits very similar friction force profiles prior to heating. This demonstrates the ability for a polymeric material with a uniform coefficient of kinetic friction to controllably transform into a material with varying properties of friction.

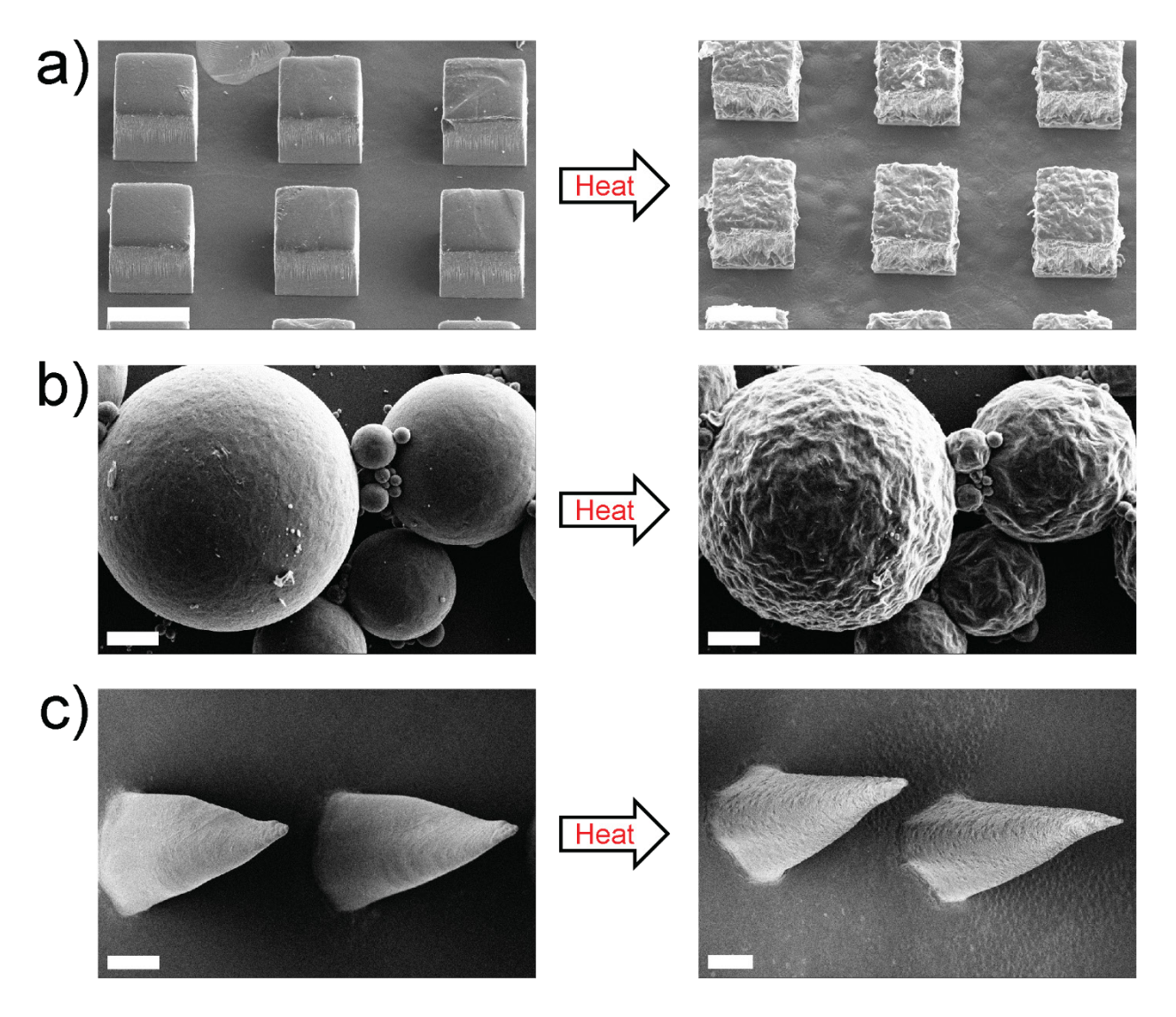


**Figure 7.** Surface deformation of microstructures. SEM micrographs of a) micro-rectangular prisms, b) microspheres, and c) microneedles demonstrating roughness after heating. Scale bars: 100 μm for micro-rectangular prisms, 50 μm for microspheres, and 200 μm for microneedles.

As aforementioned, most previously described techniques to generate polymers with dynamic roughness require some form of an initial programming procedure. Such programming procedures hinder the ability to control the surface topography of 3D structures. Here, as no programming step is required to guide crystallization during polymerization, polymeric microstructures with emergent roughness can be readily obtained. To demonstrate this versatility, (75:25:90:10)

(OTD:DAA:NDT:PETMP) samples were synthesized through three varying techniques to form microstructures, each capable of becoming rough on heating. Micro-rectangular prisms were molded by polymerization in a silicon mold (Figure 7a). Microspheres were synthesized through polymerization of an oil-in-water emulsion (Figure 7b). Microneedles were molded by soft lithography in a silicone mold (Figure 7c). After synthesizing these structures through such versatile fabrication techniques, they were subsequently heated, demonstrating controllable, significant surface deformations (Movie S5). We expect that this technique could be applied to a wide range of microstructures with applications in adhesives<sup>46,47</sup> and dynamic optical properties<sup>14,15</sup>.

#### Conclusion

In this work, we have developed a mechanism which allows for the controllable alteration of the surface topography of films and microstructures in an efficient, facile manner. This has been demonstrated in materials that undergo crystallization during photopolymerization of thiol-ene monomers. The degree of undercooling controls the degree of roughness of these polymeric surfaces. Additionally, spatiotemporal control of roughness is achieved by patterning the polymerization temperature within a single material. This enables dynamic control of the coefficient of kinetic friction. Prior to this work, initial programming steps were required to control the surface topography of polymers, thus limiting their use to flat 2D substrates. However, the process described here does not require a programming step, thus allowing for controllable surface alteration in a wide variety of microstructures. This fundamentally distinguishes this mechanism from current techniques used to control surface topography.

#### ASSOCIATED CONTENT

# **Supporting Information.**

The Supporting Information is available free of charge on the ACS Publications website at DOI:.

Table 1 and Figures S1 – S12 (PDF)

Film Surface Deformation (MP4)

Crystallization Kinetics (MP4)

Spatiotemporal Control of Surface Roughness (MP4)

Differences in the Coefficient of Friction (MP4)

Surface Deformation of Microspheres (MP4)

#### **AUTHOR INFORMATION**

# **Corresponding Author**

\*E-mail: taylor.ware@utdallas.edu

### **Notes**

The authors declare no competing financial interest.

#### ACKNOWLEDGMENT

This material is based upon work supported by the National Science Foundation under Grant No.

1663367 and 1752846.

#### References:

- (1) Assender, H.; Bliznyuk, V.; Porfyrakis, K. How Surface Topography Relates to Materials' Properties. Science. 2002, pp 973–976. https://doi.org/10.1126/science.1074955.
- Yang, J.; Lv, J.; Behl, M.; Lendlein, A.; Yang, D.; Zhang, L.; Shi, C.; Guo, J.; Feng, Y. Functionalization of Polycarbonate Surfaces by Grafting PEG and Zwitterionic Polymers with a Multicomb Structure. *Macromol. Biosci.* 2013, 13 (12), 1681–1688. https://doi.org/10.1002/mabi.201300264.
- (3) Yang, P.; Baker, R. M.; Henderson, J. H.; Mather, P. T. In Vitro Wrinkle Formation via Shape Memory Dynamically Aligns Adherent Cells. *Soft Matter* **2013**, 9 (18), 4705–4714. https://doi.org/10.1039/c3sm00024a.
- (4) Liu, D.; Broer, D. J. Light Controlled Friction at a Liquid Crystal Polymer Coating with Switchable Patterning. Soft Matter 2014, 10 (40), 7952–7958. https://doi.org/10.1039/c4sm01249f.
- (5) Hendrikx, M.; Liu, D.; Schenning, A. P. H. J.; Broer, D. J. Oscillatory Dynamic Surface Structures in Patterned Liquid Crystal Network Coatings. In *Proc. SPIE* 10735, Liquid Crystals XXII, 1073507; 2018; p 5. https://doi.org/10.1117/12.2320576.
- (6) Turner, S. A.; Zhou, J.; Sheiko, S. S.; Ashby, V. S. Switchable Micropatterned Surface Topographies Mediated by Reversible Shape Memory. ACS Appl. Mater. Interfaces 2014, 6 (11), 8017–8021. https://doi.org/10.1021/am501970d.

- (7) Brosnan, S. M.; Brown, A. H.; Ashby, V. S. It Is the Outside That Counts: Chemical and Physical Control of Dynamic Surfaces. *J. Am. Chem. Soc.* **2013**, *135* (8), 3067–3072. https://doi.org/10.1021/ja308080g.
- (8) Babakhanova, G.; Turiv, T.; Guo, Y.; Hendrikx, M.; Wei, Q. H.; Schenning, A. P. H. J.; Broer, D. J.; Lavrentovich, O. D. Liquid Crystal Elastomer Coatings with Programmed Response of Surface Profile. *Nat. Commun.* 2018, 9 (1). https://doi.org/10.1038/s41467-018-02895-9.
- (9) Guvendiren, M.; Yang, S.; Burdick, J. A. Swelling-Induced Surface Patterns in Hydrogels with Gradient Crosslinking Density. *Adv. Funct. Mater.* 2009, 19 (19), 3038–3045. https://doi.org/10.1002/adfm.200900622.
- (10) Feng, W.; Broer, D. J.; Liu, D. Oscillating Chiral-Nematic Fingerprints Wipe Away

  Dust. *Adv. Mater.* **2018**, *30* (11). https://doi.org/10.1002/adma.201704970.
- (11) Liu, D.; Tito, N. B.; Broer, D. J. Protruding Organic Surfaces Triggered by In-Plane Electric Fields. *Nat. Commun.* **2017**, *8* (1). https://doi.org/10.1038/s41467-017-01448-w.
- (12) Schäffer, E.; Thurn-Albrecht, T.; Russell, T. P.; Steiner, U. Electrically Induced Structure Formation and Pattern Transfer. *Nature* **2000**. https://doi.org/10.1038/35002540.
- (13) Chung, J. Y.; Youngblood, J. P.; Stafford, C. M. Anisotropic Wetting on Tunable Micro-Wrinkled Surfaces. Soft Matter 2007, 3 (9), 1163–1169. https://doi.org/10.1039/b705112c.

- (14) Kragt, A. J. J.; Broer, D. J.; Schenning, A. P. H. J. Easily Processable and Programmable Responsive Semi-Interpenetrating Liquid Crystalline Polymer Network Coatings with Changing Reflectivities and Surface Topographies. *Adv. Funct. Mater.* 2018, 28 (6). https://doi.org/10.1002/adfm.201704756.
- (15) Xu, H.; Yu, C.; Wang, S.; Malyarchuk, V.; Xie, T.; Rogers, J. A. Deformable, Programmable, and Shape-Memorizing Micro-Optics. *Adv. Funct. Mater.* **2013**, 23 (26), 3299–3306. https://doi.org/10.1002/adfm.201203396.
- (16) Chaudhury, M. K.; Whitesides, G. M. How to Make Water Run Uphill. *Science*.1992, 256 (5063), 1539–1541. https://doi.org/10.1126/science.256.5063.1539.
- (17) Chen, D.; Yoon, J.; Chandra, D.; Crosby, A. J.; Hayward, R. C. Stimuli-Responsive Buckling Mechanics of Polymer Films. *J. Polym. Sci. Part B Polym. Phys.* **2014**, *52* (22), 1441–1461. https://doi.org/10.1002/polb.23590.
- (18) Schweikart, A.; Horn, A.; Böker, A.; Fery, A. Controlled Wrinkling as a Novel Method for the Fabrication of Patterned Surfaces. *Adv. Polym. Sci.* **2010**, 227 (1), 75–99. https://doi.org/10.1007/12-2009-22.
- (19) Alzahrani, A. A.; Nair, D. P.; Smits, D. J.; Saed, M.; Yakacki, C. M.; Bowman, C. N. Photo-CuAAC Induced Wrinkle Formation in a Thiol-Acrylate Elastomer via Sequential Click Reactions. *Chem. Mater.* 2014, 26 (18), 5303–5309. https://doi.org/10.1021/cm502237b.
- (20) Yoo, P. J.; Suh, K. Y.; Park, S. Y.; Lee, H. H. Physical Self-Assembly of Microstructures by Anisotropic Buckling. *Adv. Mater.* **2002**, *14* (19), 1383–1387.

- https://doi.org/10.1002/1521-4095(20021002)14:19<1383::AID-ADMA1383>3.0.CO;2-D.
- (21) Bowden, N.; Brittain, S.; Evans, A. G.; Hutchinson, J. W.; Whitesides, G. M. Spontaneous Formation of Ordered Structures in Thin Films of Metals Supported on an Elastomeric Polymer. *Nature* 1998, 393 (6681), 146–149. https://doi.org/10.1038/30193.
- (22) Tallinen, T.; Biggins, J. S. Mechanics of Invagination and Folding: Hybridized Instabilities When One Soft Tissue Grows on Another. *Phys. Rev. E - Stat. Nonlinear, Soft Matter Phys.* 2015, 92 (2), 1–8. https://doi.org/10.1103/PhysRevE.92.022720.
- (23) Lendlein, A.; Jiang, H.; Jünger, O.; Langer, R. Light-Induced Shape-Memory Polymers. *Nature* **2005**, *434* (7035), 879–882. https://doi.org/10.1038/nature03496.
- (24) Balk, M.; Behl, M.; Nöchel, U.; Lendlein, A. Shape-Memory Hydrogels with Switching Segments Based on Oligo(ω-Pentadecalactone). *Macromol. Mater. Eng.* 2012, 297 (12), 1184–1192. https://doi.org/10.1002/mame.201200232.
- (25) Xie, T. Tunable Polymer Multi-Shape Memory Effect. *Nature* **2010**, *464* (7286), 267–270. https://doi.org/10.1038/nature08863.
- (26) Ware, T. H.; McConney, M. E.; Wie, J. J.; Tondiglia, V. P.; White, T. J. Voxelated Liquid Crystal Elastomers. Science. 2015, 347 (6225), 982–984. https://doi.org/10.1126/science.1261019.

- (27) Hoyle, C. E.; Bowman, C. N. Thiol-Ene Click Chemistry. *Angew. Chemie Int. Ed.*2010, 49 (9), 1540–1573. https://doi.org/10.1002/anie.200903924.
- (28) Blaine, R. L. Determination of Polyethylene Crystallinity by DSC. *China Plast.* **2002**, 2002 (09), 1–3.
- (29) Kanafi, M. M. 1-Dimensional Surface Roughness Power Spectrum of a Profile or Topography. *MATLAB Central File Exchange*. 2020.
- (30) Mwema, F. M.; Akinlabi, E. T.; Oladijo, O. P.; Oladijo, O. P. The Use of Power Spectrum Density for Surface Characterization of Thin Films. *Photoenergy Thin Film Mater.* **2019**, 379–411. https://doi.org/10.1002/9781119580546.ch9.
- (31) Wang, Q. L.; Zhu, D. D.; Chen, Y.; Guo, X. D. A Fabrication Method of Microneedle Molds with Controlled Microstructures. *Mater. Sci. Eng. C* 2016, 65, 135–142. https://doi.org/10.1016/j.msec.2016.03.097.
- (32) Childress, K. K.; Alim, M. D.; Hernandez, J. J.; Stansbury, J. W.; Bowman, C. N. Additive Manufacture of Lightly Crosslinked Semicrystalline Thiol-Enes for Enhanced Mechanical Performance. *Polym. Chem.* 2019. https://doi.org/10.1039/c9py01452g.
- (33) Surendran, G.; Gazicki, M.; James, W. J.; Yasuda, H. Polymerization of Para-Xylylene Derivatives. V. Effects of the Sublimation Rate of Di-p-Xylylene on the Crystallinity of Parylene C Deposited at Different Temperatures. *J. Polym. Sci. Part A Polym. Chem.* 1987, 25 (8), 2089–2106. https://doi.org/10.1002/pola.1987.080250806.

- (34) Kubo, S.; Wunderlich, B. Crystallization during Polymerization of Poly-p-Xylylene.
  J. Polym. Sci. Part A-2 Polym. Phys. 1972, 10 (10), 1949–1966.
  https://doi.org/10.1002/pol.1972.180101007.
- (35) Wunderlich, B. Crystallization during Polymerization. In Fortschritte der Hochpolymeren-Forschung; Springer-Verlag: Berlin/Heidelberg, 1968; pp 568– 619. https://doi.org/10.1007/BFb0051119.
- (36) Zia, Q.; Androsch, R.; Radusch, H. J.; Ingoliç, E. Crystal Morphology of Rapidly Cooled Isotactic Polypropylene: A Comparative Study by TEM and AFM. *Polym. Bull.* 2008, 60 (6), 791–798. https://doi.org/10.1007/s00289-008-0908-8.
- (37) Piccarolo, S. Morphological Changes in Isotactic Polypropylene as a Function of Cooling Rate. *J. Macromol. Sci. Part B* **1992**, *31* (4), 501–511. https://doi.org/10.1080/00222349208215467.
- (38) Zia, Q.; Androsch, R.; Radusch, H. J.; Piccarolo, S. Morphology, Reorganization and Stability of Mesomorphic Nanocrystals in Isotactic Polypropylene. *Polymer* (*Guildf*). **2006**, *47* (24), 8163–8172. https://doi.org/10.1016/j.polymer.2006.09.038.
- (39) Compton, B. G.; Post, B. K.; Duty, C. E.; Love, L.; Kunc, V. Thermal Analysis of Additive Manufacturing of Large-Scale Thermoplastic Polymer Composites. *Addit. Manuf.* 2017, 17, 77–86. https://doi.org/10.1016/j.addma.2017.07.006.
- (40) Love, L. J.; Kunc, V.; Rios, O.; Duty, C. E.; Elliott, A. M.; Post, B. K.; Smith, R. J.; Blue, C. A. The Importance of Carbon Fiber to Polymer Additive Manufacturing. *J. Mater. Res.* 2014, 29 (17), 1893–1898. https://doi.org/10.1557/jmr.2014.212.

- (41) Ligon, S. C.; Liska, R.; Stampfl, J.; Gurr, M.; Mülhaupt, R. Polymers for 3D Printing and Customized Additive Manufacturing. *Chem. Rev.* **2017**, *117* (15), 10212–10290. https://doi.org/10.1021/acs.chemrev.7b00074.
- (42) Thomas, C.; Seguela, R.; Detrez, F.; Miri, V.; Vanmansart, C. Plastic Deformation of Spherulitic Semi-Crystalline Polymers: An in Situ AFM Study of Polybutene under Tensile Drawing. *Polymer (Guildf)*. **2009**, *50* (15), 3714–3723. https://doi.org/10.1016/j.polymer.2009.06.023.
- (43) Beng, N.; Minn, T. M.; Sinha, S. K. A Tribological Study of SU-8 Micro-Dot Patterns
  Printed on Si Surface in a Flat-on-Flat Reciprocating Sliding Test. *Tribol. Lett.* **2011**,

  44 (2), 167–176. https://doi.org/10.1007/s11249-011-9835-1.
- (44) He, B.; Chen, W.; Jane Wang, Q. Surface Texture Effect on Friction of a Microtextured Poly(Dimethylsiloxane) (PDMS). *Tribol. Lett.* 2008, 31 (3), 187–197. https://doi.org/10.1007/s11249-008-9351-0.
- (45) Liu, D.; Broer, D. J. Self-Assembled Dynamic 3D Fingerprints in Liquid-Crystal Coatings Towards Controllable Friction and Adhesion. *Angew. Chemie* 2014, 126 (18), 4630–4634. https://doi.org/10.1002/ange.201400370.
- (46) Chen, C. M.; Chiang, C. L.; Lai, C. L.; Xie, T.; Yang, S. Buckling-Based Strong Dry Adhesives via Interlocking. *Adv. Funct. Mater.* **2013**, 23 (30), 3813–3823. https://doi.org/10.1002/adfm.201300052.
- (47) Kim, S.; Sitti, M.; Xie, T.; Xiao, X. Reversible Dry Micro-Fibrillar Adhesives with Thermally Controllable Adhesion. *Soft Matter* **2009**, *5* (19), 3689–3693.

https://doi.org/10.1039/b909885b.

# For Table of Contents use only

# Emergent Surface Topography Enabled by Concurrent Crystallization and Polymerization

Mustafa K. Abdelrahman<sup>†</sup>, Hyun Kim<sup>†,‡</sup>, Jimin Maeng<sup>†</sup>, Patrick Ondrusek<sup>†</sup>, Taylor H. Ware<sup>\*,†</sup>

<sup>†</sup>Department of Bioengineering, The University of Texas at Dallas, 800 W Campbell Rd., Richardson, Texas 75080, United States

<sup>‡</sup> Current Address: Sensors and Electron Devices Directorate, CCDC Army Research Laboratory, 2800 Powder Mill Rd., Adelphi, Maryland 20783, United States

